

## GREENHOUSE GASES

# High-temperature carbon dioxide capture in a porous material with terminal zinc hydride sites

Rachel C. Rohde<sup>1,2†</sup>, Kurtis M. Carsch<sup>1,2†</sup>, Matthew N. Dods<sup>1,3</sup>, Henry Z. H. Jiang<sup>1,2,4</sup>, Alexandra R. McIsaac<sup>2,5</sup>, Ryan A. Klein<sup>6,7</sup>, Hyunchul Kwon<sup>1,2</sup>, Sarah L. Karstens<sup>1,2,4</sup>, Yang Wang<sup>1,3</sup>, Adrian J. Huang<sup>1,2,4</sup>, Jordan W. Taylor<sup>2</sup>, Yuto Yabuuchi<sup>1,2,4</sup>, Nikolay V. Tkachenko<sup>1,2,4</sup>, Katie R. Meihaus<sup>1,2</sup>, Hiroyasu Furukawa<sup>1,2,4</sup>, Danielle R. Yahne<sup>8</sup>, Kaitlyn E. Engler<sup>3,4</sup>, Karen C. Bustillo<sup>9</sup>, Andrew M. Minor<sup>9,10</sup>, Jeffrey A. Reimer<sup>1,3,4</sup>, Martin Head-Gordon<sup>1,2,5</sup>, Craig M. Brown<sup>6,11</sup>, Jeffrey R. Long<sup>1,2,3,4,10\*</sup>

Carbon capture can mitigate point-source carbon dioxide (CO<sub>2</sub>) emissions, but hurdles remain that impede the widespread adoption of amine-based technologies. Capturing CO<sub>2</sub> at temperatures closer to those of many industrial exhaust streams (>200°C) is of interest, although metal oxide adsorbents that operate at these temperatures typically exhibit sluggish CO<sub>2</sub> absorption kinetics and instability to cycling. Here, we report a porous metal–organic framework featuring terminal zinc hydride sites that reversibly bind CO<sub>2</sub> at temperatures above 200°C—conditions that are unprecedented for intrinsically porous materials. Gas adsorption, structural, spectroscopic, and computational analyses elucidate the rapid, reversible nature of this transformation. Extended cycling and breakthrough analyses reveal that the material is capable of deep carbon capture at low CO<sub>2</sub> concentrations and high temperatures relevant to postcombustion capture.

Carbon capture technology is an essential strategy to limit global warming (1, 2). Although the use of renewable energy sources is accelerating (3), fossil fuels are still projected to supply most of the global power over the next few decades (4–6). Postcombustion CO<sub>2</sub> capture with aqueous amines is the most mature technology (7, 8), although the high heat capacities, corrosivity, and volatility of these solutions have thus far precluded their widespread adoption (9). Additionally, given the relatively low temperatures at which aqueous amines react with CO<sub>2</sub> (≤60°C), their use would require that many target high-temperature effluent streams—such as those generated from steel and cement making (>200°C)—be cooled substantially before CO<sub>2</sub> capture, adding sizably to capital and operational costs.

Postcombustion capture of CO<sub>2</sub> at higher temperatures, closer to those of many exhaust streams, could minimize or obviate the need

for such cooling and facilitate the recuperation of quality heat generated upon exothermic CO<sub>2</sub> uptake (10–12) (fig. S1). This possibility has motivated the study of dense metal oxide adsorbents that can react with CO<sub>2</sub> to form metal carbonates at high temperatures (~150° to 1200°C). However, such materials tend to deactivate over the course of extended cycling as a result of large changes in volume that occur during carbonate formation, which contribute to particle sintering (13–15).

Metal–organic frameworks (MOFs) are another class of materials that have been intensively studied for CO<sub>2</sub> capture applications (16). These crystalline solids feature chemically robust, intrinsically porous scaffolds that are not altered by CO<sub>2</sub> binding, and as such, they can exhibit rapid adsorption kinetics and exceptional stability to long-term cycling. Such properties are well exemplified by MOFs with metal sites appended with polyamines, which have emerged as leading candidates for CO<sub>2</sub> capture (17), although MOFs have not yet been shown to effectively capture CO<sub>2</sub> at temperatures above ~150°C (17–21). The realization of a framework that could capture CO<sub>2</sub> at more-elevated temperatures could drastically expand the potential application space for these promising adsorbents.

In polyamine-appended MOFs, CO<sub>2</sub> reversibly inserts into the metal–amine bonds to form ammonium carbamate species. Another example of CO<sub>2</sub> insertion chemistry is the reaction of CO<sub>2</sub> with metal hydrides to form metal formates, which is well established in molecular literature (22) and a subject of interest in the search for sustainable routes to CO<sub>2</sub> utilization (23, 24). The reverse reaction was reported for the MOF Zn<sub>5</sub>(O<sub>2</sub>CH)<sub>4</sub>Cl<sub>4-x</sub>(btdd)<sub>3</sub> [Zn(O<sub>2</sub>CH)-MFU-4l; H<sub>2</sub>btdd = bis(1*H*-1,2,3-triazolo[4,5-*b*,

[4',5'-*i*])dibenzo[1,4]dioxin; MFU-4l = Zn<sub>5</sub>Cl<sub>4</sub>(btdd)<sub>3</sub>], which evolves CO<sub>2</sub> at temperatures above 200°C to form ZnH-MFU-4l [Zn<sub>5</sub>H<sub>2</sub>Cl<sub>4-x</sub>(btdd)<sub>3</sub>; Fig. 1A] (25). Here, we show that ZnH-MFU-4l is likewise capable of reversibly capturing CO<sub>2</sub> to form Zn(O<sub>2</sub>CH)-MFU-4l, but notably, this chemistry occurs between ~200° and 400°C (Fig. 1B). In situ structural and spectroscopic data confirm the quantitative nature of this insertion mechanism, while extended CO<sub>2</sub> adsorption–desorption cycling, breakthrough, and kinetic analyses highlight the robustness of this mechanism and its potential relevance to CO<sub>2</sub> capture from a diverse array of point sources.

## Synthesis and preliminary characterization

The framework ZnH-MFU-4l was previously synthesized from MFU-4l (hereafter, ZnCl-MFU-4l) (26) through formate exchange to generate Zn(O<sub>2</sub>CH)-MFU-4l, followed by thermolysis at 300°C to drive off CO<sub>2</sub> (25). In our hands, this preparation yielded ZnH-MFU-4l with hydride estimated to occupy 73% of the peripheral zinc(II) sites, as indicated by <sup>1</sup>H nuclear magnetic resonance (NMR) spectroscopy analysis of a digested sample of the Zn(O<sub>2</sub>CH)-MFU-4l precursor (fig. S64). Seeking to optimize

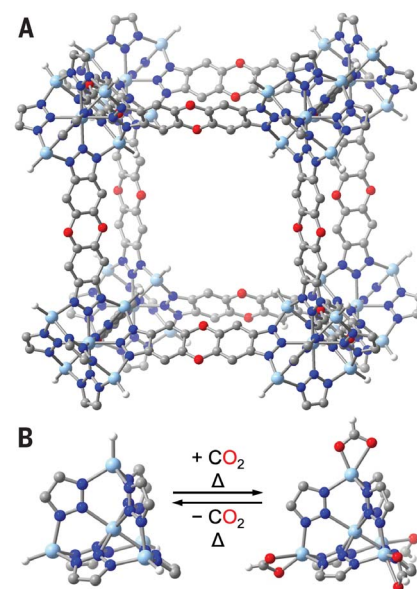


**Fig. 1. Reversible high-temperature CO<sub>2</sub> capture in a zinc hydride MOF.**

(A) A portion of the structure of ZnH-MFU-4l, as determined from single-crystal x-ray diffraction analysis. (B) (Left) Expanded view of a pentanuclear cluster node of the framework [ $d_{\text{Zn-H}} = 1.546(9)$  Å,  $\text{N-Zn-H} = 121.2(4)^\circ$ ; table S20]. (Right) At temperatures above 200°C, CO<sub>2</sub> reversibly inserts into the Zn–H bonds of ZnH-MFU-4l to generate Zn–formate species [ $d_{\text{Zn-O}} = 1.971(6)$  and  $2.408(4)$  Å,  $\text{O-C-O} = 119.2(6)^\circ$ ; table S21]. Light-blue, gray, blue, red, and white spheres represent Zn, C, N, O, and H atoms, respectively.

<sup>1</sup>Institute for Decarbonization Materials, University of California, Berkeley, CA 94720, USA. <sup>2</sup>Department of Chemistry, University of California, Berkeley, CA 94720, USA. <sup>3</sup>Department of Chemical and Biomolecular Engineering, University of California, Berkeley, CA 94720, USA. <sup>4</sup>Materials Sciences Division, Lawrence Berkeley National Laboratory, Berkeley, CA 94720, USA. <sup>5</sup>Chemical Sciences Division, Lawrence Berkeley National Laboratory, Berkeley, CA 94720, USA. <sup>6</sup>Center for Neutron Research, National Institute of Standards and Technology, Gaithersburg, MD 20899, USA. <sup>7</sup>Material, Chemical, and Computational Sciences Directorate, National Renewable Energy Laboratory, Golden, CO 80401, USA. <sup>8</sup>Neutron Scattering Division, Oak Ridge National Laboratory, Oak Ridge, TN 37831, USA. <sup>9</sup>National Center for Electron Microscopy, Molecular Foundry, Lawrence Berkeley National Laboratory, Berkeley, CA 94720, USA. <sup>10</sup>Department of Materials Science and Engineering, University of California, Berkeley, CA 94720, USA. <sup>11</sup>Chemical and Biomolecular Engineering, University of Delaware, Newark, DE 19716, USA. \*Corresponding author. Email: jrlong@berkeley.edu †These authors contributed equally to this work.

the zinc hydride loading, we devised an alternative synthesis involving alkylation of ZnCl-MFU-4l with diethylzinc to access ZnEt-MFU-4l (27), followed by protonolysis with formic acid to yield Zn(O<sub>2</sub>CH)-MFU-4l [see section 3.6 of the supplementary materials (SM)]. Heating the zinc formate framework under dynamic vacuum or N<sub>2</sub> afforded ZnH-MFU-4l as an off-white, microcrystalline powder.

Energy-dispersive x-ray spectroscopy analysis of the Zn and Cl content in ZnH-MFU-4l revealed that a small fraction (6%) of the zinc (II) sites remained coordinated by chloride, giving the formula unit Zn<sub>5</sub>H<sub>3.76</sub>Cl<sub>0.24</sub>(btdd)<sub>3</sub> (fig. S54), and analysis of N<sub>2</sub> adsorption data obtained at 77 K revealed a high Brunauer-Emmett-Teller surface area of 3920(70) m<sup>2</sup>/g (fig. S2). The infrared spectrum of the material features a diagnostic Zn–H vibration at 1792 cm<sup>−1</sup> (25) ( $\nu_{\text{Zn-H}} = 1289 \text{ cm}^{-1}$ , compared with 1277 cm<sup>−1</sup> for a simple harmonic oscillator; fig. S70). We also devised an alternative synthesis of ZnH-MFU-4l that can be performed in air without the exclusion of water (see section 3.8 of the SM for details). However, the number of hydride sites in ZnH-MFU-4l prepared through this approach was found to be slightly lower [Zn<sub>5</sub>H<sub>3.5</sub>Br<sub>0.5</sub>(btdd)<sub>3</sub> as indicated by <sup>1</sup>H NMR spectroscopy analysis; fig. S57]. Thus, all subsequent analyses were performed with material prepared through the alkylation and protonolysis route.

Through a series of single-crystal-to-single-crystal transformations starting from ZnCl-MFU-4l, we isolated crystals of ZnH-MFU-4l suitable for x-ray diffraction analysis (Fig. 1B; see section 3.11 of the SM). The terminal hydride ligand was located in the Fourier difference map, and refinement against the electron density data yielded a Zn–H bond length of 1.546(9) Å. Neutron powder diffraction data collected at 7 K further support the presence of a hydride, and Rietveld refinement of these data yielded a Zn–H bond length of 1.56(2) Å (see section 11.1 of the SM and table S23), consistent with the single-crystal x-ray diffraction data. These distances are within the range of reported Zn–H distances for various molecular compounds [1.44(3) to 1.75(3) Å] (28).

Although the stability of ZnH-MFU-4l to atmosphere and moisture was not previously reported, we found that it is robust in ambient air at ambient temperature for at least 18 months, as indicated by powder x-ray diffraction and infrared analyses (figs. S82 and S72). Thermogravimetric analysis (TGA) data collected for ZnH-MFU-4l under pure N<sub>2</sub> revealed that the framework is also thermally robust and stable up to ~450°C (fig. S29); decarboxylation of Zn(O<sub>2</sub>CH)-MFU-4l to give ZnH-MFU-4l occurred above 180°C under N<sub>2</sub> (25). Notably, TGA data collected for Zn(O<sub>2</sub>CH)-MFU-4l under an atmosphere of pure CO<sub>2</sub> showed only a gradual decline in sample mass up to

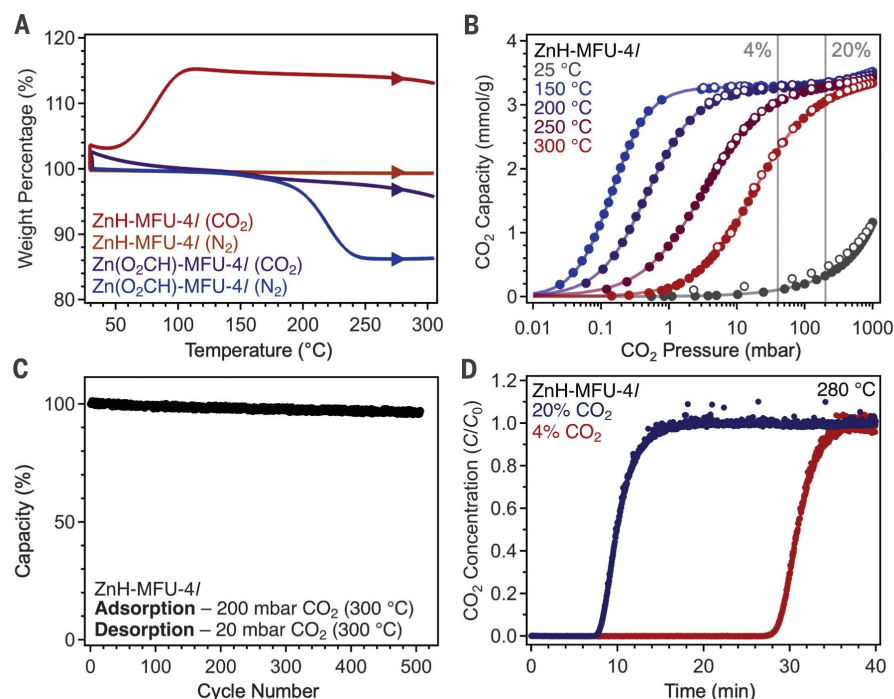


**Fig. 2. High-temperature isobaric and isothermal CO<sub>2</sub> adsorption data for ZnH-MFU-4l.**

(A) Thermogravimetric analysis data collected for ZnH-MFU-4l or Zn(O<sub>2</sub>CH)-MFU-4l under an atmosphere of pure CO<sub>2</sub> or N<sub>2</sub>. (B) Variable-temperature CO<sub>2</sub> adsorption (filled circles) and desorption (open circles) isotherms for ZnH-MFU-4l. Solid lines are guides for the eyes. Vertical lines denote CO<sub>2</sub> concentrations relevant to flue streams produced from natural gas combine cycles and single-cycle turbines (~4% CO<sub>2</sub>) and cement and steelmaking (20% CO<sub>2</sub> and higher) (18, 32, 33). (C) Cycling data for ZnH-MFU-4l during the course of 508 isothermal adsorption (200 mbar CO<sub>2</sub>) and desorption under vacuum (20 mbar CO<sub>2</sub>) cycles at 300°C, plotted as a percentage of the capacity measured for the first cycle (1.24 mmol/g). Note that the chosen desorption pressure would achieve only partial CO<sub>2</sub> desorption, and the measured capacities are consistent with those expected with this desorption pressure, as indicated by the isothermal data. The capacity in the final cycle was 1.19 mmol/g. See section 2.4 of the SM for experimental details and fig. S27 for the raw data. (D) Breakthrough data collected for a pelletized sample of ZnH-MFU-4l exposed to a flowing (10 sccm) gas stream at ~280°C consisting of 20% CO<sub>2</sub> in N<sub>2</sub> (blue data) or 4% CO<sub>2</sub> in N<sub>2</sub> (red data). See sections 2.8 and 7 of the SM for experimental details.

300°C, indicating that decarboxylation was suppressed under these conditions (Fig. 2A). In contrast, in the TGA data collected for ZnH-MFU-4l under pure CO<sub>2</sub>, there was an initial small mass increase followed by a near plateau until about 50°C, after which point the mass monotonically increased until 100°C and was relatively constant up to 300°C. Above 110°C, the profile for ZnH-MFU-4l mirrored that of Zn(O<sub>2</sub>CH)-MFU-4l, suggesting that the mass increase was associated with CO<sub>2</sub> insertion into the Zn–H units to yield Zn(O<sub>2</sub>CH)-MFU-4l. Data collected for ZnH-MFU-4l under an atmosphere of only 20% CO<sub>2</sub> in N<sub>2</sub> displayed a similar profile (fig. S30).

#### CO<sub>2</sub> adsorption properties and isothermal operation at elevated temperatures

Single-component CO<sub>2</sub> adsorption isotherms were collected between 25° and 300°C to further investigate the temperature-dependent CO<sub>2</sub>

adsorption properties of ZnH-MFU-4l (Fig. 2B and fig. S15). At 25° and 50°C, CO<sub>2</sub> uptake occurred in a gradual, monotonic fashion, and the material achieved capacities of 1.16 and 1.15 mmol/g, respectively, at 1 bar. However, at 100°C, the low-pressure uptake was very steep, indicative of strong binding of CO<sub>2</sub> within the framework, and the material achieved a capacity of 3.23 mmol/g at 1 bar. Such a drastic increase in CO<sub>2</sub> capacity with increasing temperature has not previously been reported for MOFs, which generally exhibit CO<sub>2</sub> capacities that decrease monotonically upon heating from ambient temperatures (17, 19, 26, 27, 29, 30).

Increasing the temperature further resulted in yet steeper CO<sub>2</sub> uptake at low pressures and higher capacities overall. At 150°C, the material achieved a capacity of 3.27 mmol/g at only 10 mbar, near the predicted capacity of 3.3 mmol/g if one molecule of CO<sub>2</sub> were to bind at each of the zinc hydride sites (see



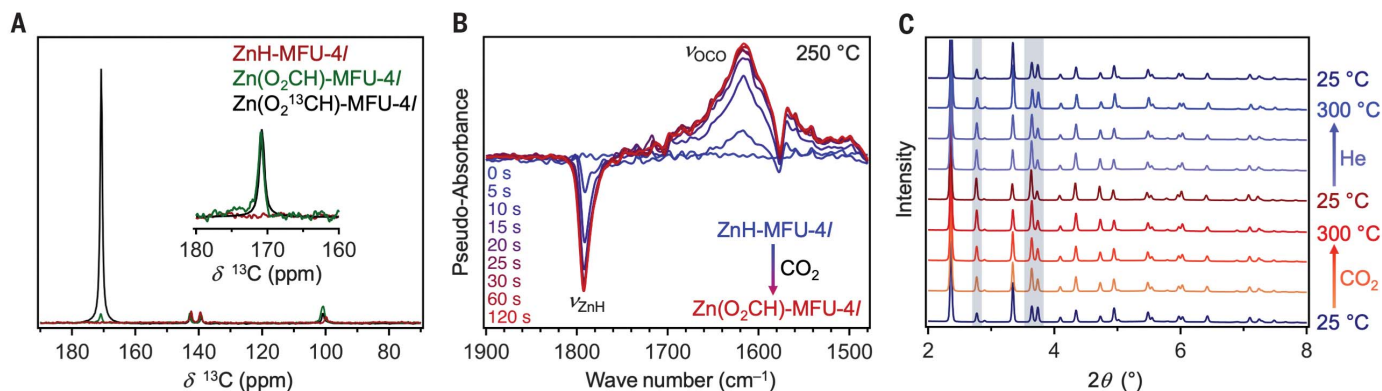


**Fig. 3. Spectroscopic and structural characterization of reversible CO<sub>2</sub> uptake in ZnH-MFU-4l.**

**(A)** Solid-state  $^{13}\text{C}\{^1\text{H}\}$  cross polarization NMR spectra (magic angle spin rates of 20 kHz) for ZnH-MFU-4l, Zn(O<sub>2</sub>CH)-MFU-4l, and ZnH-MFU-4l dosed with 1 bar  $^{13}\text{CO}_2$  at  $\sim 280^\circ\text{C}$ , revealing a peak at 170.8 ppm corresponding to formate in Zn(O<sub>2</sub>CH)-MFU-4l and Zn(O<sub>2</sub> $^{13}\text{CH}$ )-MFU-4l. The inset depicts the intensity-normalized formate  $^{13}\text{C}$  resonance. **(B)** Difference spectra obtained from subtracting time-resolved DRIFTS data for a sample of ZnH-MFU-4l dosed in situ with 200 mbar CO<sub>2</sub> at  $250^\circ\text{C}$  from a spectrum collected for ZnH-MFU-4l at  $250^\circ\text{C}$  ( $t = 0$  corresponds to a spectrum collected immediately before dosing). **(C)** Representative powder x-ray diffraction patterns

collected during the course of the in situ gas-dosing experiment. Starting from a sample of ZnH-MFU-4l cooled from  $300^\circ$  to  $25^\circ\text{C}$  under He (bottom blue trace), diffraction patterns ( $\lambda = 0.45207 \text{ \AA}$ ) were collected for ZnH-MFU-4l during the course of heating from  $25^\circ$  to  $300^\circ\text{C}$  and then cooling under flowing CO<sub>2</sub> (10 sccm, orange to dark-red traces); heating from  $25^\circ$  to  $300^\circ\text{C}$  under He to desorb CO<sub>2</sub>; and finally cooling to  $25^\circ\text{C}$  under He (10 sccm; blue traces). Rietveld refinements of the top and bottom patterns indicate that the structure of ZnH-MFU-4l is the same after cycling. Select patterns are shown to highlight changes with heating under the different gas atmospheres. Highlighted reflections are diagnostic of structural changes. Additional diffraction patterns are provided in fig. S86.

section 2.12 and table S4 of the SM for volumetric uptakes). At higher pressures, the uptake began to plateau and reached a value of 3.52 mmol/g at 1 bar. Steep CO<sub>2</sub> uptake likewise occurred at  $200^\circ$ ,  $250^\circ$ , and  $300^\circ\text{C}$ , and at these temperatures, the material achieved a capacity of 3.27 mmol/g at pressures of 65, 200, and 600 mbar, respectively. We also note that CO<sub>2</sub> could be fully desorbed from ZnH-MFU-4l at these elevated temperatures without hysteresis (Fig. 2B).

A dual-site Langmuir-Freundlich model was used to fit CO<sub>2</sub> adsorption isotherms obtained for ZnH-MFU-4l at  $280^\circ$ ,  $290^\circ$ , and  $300^\circ\text{C}$  (fig. S13 and table S5), and the corresponding simultaneous fit parameters were used with the Clausius-Clapeyron equation to determine the isosteric enthalpy ( $\Delta H_{\text{ads}}$ ) of CO<sub>2</sub> adsorption as a function of loading (fig. S24). At low loadings,  $\Delta H_{\text{ads}} = -93(\text{kJ/mol})$  and remained relatively constant up to a loading of  $\sim 2.7$  mmol/g, consistent with strong CO<sub>2</sub> chemisorption at the isolated Zn-H sites in ZnH-MFU-4l. This CO<sub>2</sub> adsorption enthalpy is among the largest values reported to date for MOFs (16, 31, 32). Similar adsorption enthalpies have been reported for certain polyamine-appended MOFs and amine-impregnated silicas (17, 21, 33). However, we note that such materials very likely exhibit higher structural degrees of freedom than ZnH-MFU-4l, owing to the variable conformations that flexible alkylamine chains can adopt before CO<sub>2</sub> adsorption (34, 35); in turn, these higher structural degrees of freedom are expected to contribute to much larger entropic penalties for

CO<sub>2</sub> binding than in the case of ZnH-MFU-4l (table S5).

No other porous solid has been reported to capture CO<sub>2</sub> at such elevated temperatures, and there are limited CO<sub>2</sub> uptake data reported for any porous adsorbent above  $100^\circ\text{C}$ . To our knowledge, the only comparable data are CO<sub>2</sub> isotherms for Mg<sub>2</sub>(dobdc) (dobdc $^{4-}$  = 1,4-dioxido-2,5-benzenedicarboxylate; Mg-MOF-74) and zeolite 13X collected at  $200^\circ\text{C}$  (36, 37), and the measured CO<sub>2</sub> capacity of 3.47 mmol/g for ZnH-MFU-4l at  $200^\circ\text{C}$  and 1 bar far exceeds reported capacities for those materials under the same conditions (0.85 and 0.54 mmol/g, respectively).

As a result of their much lower operating temperatures, MOFs reported previously have been investigated primarily for postcombustion CO<sub>2</sub> capture from flue gas generated from coal power and natural gas combined cycle plants (17, 20). In contrast, the elevated temperatures at which ZnH-MFU-4l adsorbs CO<sub>2</sub> suggests applications previously inaccessible for MOFs, such as CO<sub>2</sub> capture directly from emissions generated from iron and steelmaking (blast furnace exhaust at ambient pressure containing 21% CO<sub>2</sub> at  $300^\circ\text{C}$ ) (38) and the cement industry ( $300^\circ\text{C}$  exhaust stream at  $\sim 1$  bar with 30% CO<sub>2</sub>) (39). Additionally, the high CO<sub>2</sub> capacities achieved by ZnH-MFU-4l at very low CO<sub>2</sub> concentrations suggest that it may be a promising candidate for postcombustion CO<sub>2</sub> capture from the exhaust streams generated by natural-gas turbines ( $\sim 4\%$  CO<sub>2</sub>) (40).

Further, ZnH-MFU-4l is only one member of a potential family of frameworks featuring

zinc hydride sites capable of high-temperature CO<sub>2</sub> capture. For example, starting from the related material CFA-1 [Zn<sub>5</sub>(OAc)<sub>4</sub>(bibta)<sub>3</sub>; H<sub>2</sub>bibta = 1*H*,1'*H*-5,5'-bibenzo[*d*][1,2,3]triazole] (41), which features the flexible and less costly (42) bibta $^{2-}$  linker in place of btdd $^{2-}$ , we synthesized ZnH-CFA-1 (see section 3.14 of the SM). Like ZnH-MFU-4l, this framework also captures CO<sub>2</sub> reversibly at  $250^\circ\text{C}$  (figs. S20 and S37). The most prominent class of materials that captures CO<sub>2</sub> at comparable temperatures are MgO-based absorbents; however, the CO<sub>2</sub> capture properties of these solids have been studied primarily under pure or high concentrations of CO<sub>2</sub> and often at elevated pressures, which are conditions more relevant to precombustion capture applications (13, 43).

### Structural and spectroscopic investigation of the CO<sub>2</sub> adsorption mechanism

We investigated the mechanism of CO<sub>2</sub> uptake in ZnH-MFU-4l using x-ray diffraction and solid-state NMR spectroscopy. Single-crystal x-ray diffraction analysis of crystals of ZnH-MFU-4l dosed with 200 mbar CO<sub>2</sub> at  $200^\circ\text{C}$  for 10 min revealed conversion to Zn(O<sub>2</sub>CH)-MFU-4l, confirming that the CO<sub>2</sub> uptake in ZnH-MFU-4l occurs through CO<sub>2</sub> insertion into the Zn-H bonds (Fig. 1B and fig. S95). Solid-state  $^{13}\text{C}$  magic-angle-spinning NMR spectra (obtained by cross-polarization from  $^1\text{H}$ ) were collected for Zn(O<sub>2</sub>CH)-MFU-4l, ZnH-MFU-4l, and a sample of ZnH-MFU-4l dosed with  $\sim 1$  bar  $^{13}\text{CO}_2$  at  $280^\circ\text{C}$  (Fig. 3A). Peaks at 100.9, 139.3, and 142.8 parts per million (ppm) in all three spectra were assigned

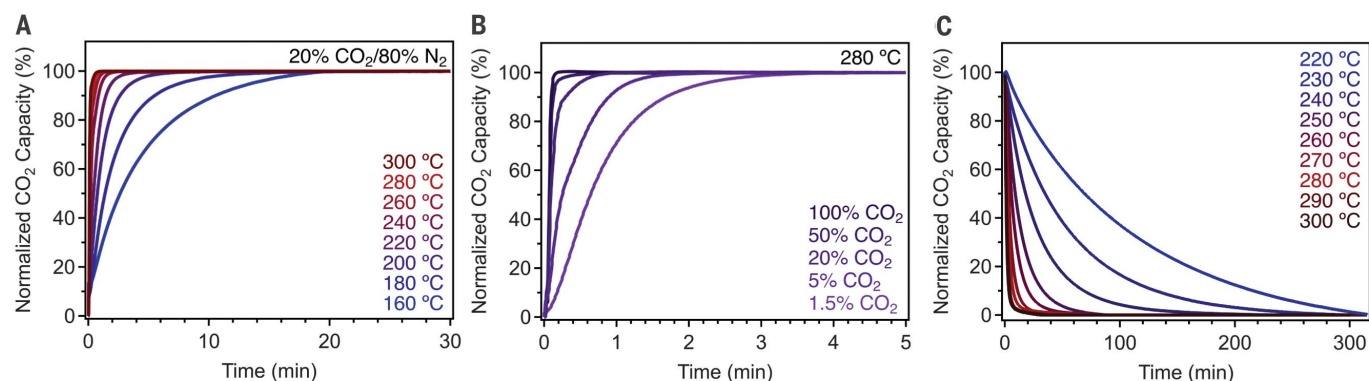


**Fig. 4. Kinetics of CO<sub>2</sub> adsorption and desorption.** (A) Kinetic adsorption profiles collected for ZnH-MFU-4l exposed to a flowing 20% CO<sub>2</sub> stream with N<sub>2</sub> balance at ~1 bar and temperatures ranging from 160° to 300°C (see section 2.13.2 of the SM for details). Saturation with CO<sub>2</sub> occurred more rapidly as the temperature of the gas stream was increased. (B) Kinetic adsorption profiles collected for ZnH-MFU-4l at 280°C exposed to flowing gas streams

(~1 bar) with CO<sub>2</sub> concentrations ranging from 1.5% CO<sub>2</sub> (balance N<sub>2</sub>) to 100% CO<sub>2</sub>. Saturation with CO<sub>2</sub> occurred more rapidly as the concentration of CO<sub>2</sub> was increased. (C) Variable-temperature kinetic desorption profiles collected for Zn(O<sub>2</sub>CH)-MFU-4l under flowing N<sub>2</sub> (see section 2.13.4 of the SM for details). All measurements were conducted under a flow rate of 100 sccm with a thermogravimetric analyzer.

to the btdd<sup>2-</sup> linker, and a <sup>13</sup>C resonance at 170.8 ppm in the spectra for Zn(O<sub>2</sub>CH)-MFU-4l and Zn(O<sub>2</sub><sup>13</sup>CH)-MFU-4l was assigned to the carbon atom of the bound formate. In the solid-state <sup>1</sup>H NMR spectrum of Zn(O<sub>2</sub>CH)-MFU-4l (fig. S68), the formate C-H resonance is located at 8.9 ppm. This feature is split into two resonances at 8.6 and 9.1 ppm in Zn(O<sub>2</sub><sup>13</sup>CH)-MFU-4l owing to *j*-coupling with <sup>13</sup>C of ~190 Hz, consistent with a previously reported formate *j*-coupling value of 195 Hz (44) and supported by <sup>13</sup>C{<sup>1</sup>H} CP-HETCOR (cross-polarization heteronuclear correlation) data (fig. S69).

In situ diffuse reflectance infrared Fourier transfer spectroscopy (DRIFTS) data collected for ZnH-MFU-4l exposed to 200 mbar dry CO<sub>2</sub> at 250°C support the reversible and rapid nature of the CO<sub>2</sub> insertion mechanism. Time-resolved difference spectra were generated by subtracting the evolving spectra collected for the CO<sub>2</sub>-dosed sample from the spectrum of ZnH-MFU-4l at 250°C (Fig. 3B and fig. S76). During a span of 1 min, broad positive vibration peaks grew in at 1613 and 2863 cm<sup>-1</sup>, which we assigned to formate C=O and C-H vibrations, respectively, concomitant with disappearance of a Zn-H vibration at 1792 cm<sup>-1</sup>, indicating the conversion of ZnH-MFU-4l to Zn(O<sub>2</sub>CH)-MFU-4l.

In situ DRIFTS data were also collected for ZnH-MFU-4l under conditions designed to demonstrate the reversibility of CO<sub>2</sub> insertion at 300°C (see fig. S77 for full assignment of features). In brief, activated ZnH-MFU-4l was dosed with 200 mbar CO<sub>2</sub> at 300°C, which resulted in near-complete disappearance of the  $\nu_{\text{Zn-H}}$  feature at 1792 cm<sup>-1</sup> and appearance of new features associated with the formate at 1613 and 2863 cm<sup>-1</sup>. The material was then regenerated isothermally under vacuum (see section 8.4 of the SM and fig. S77 for details),

which resulted in complete recovery of the  $\nu_{\text{Zn-H}}$  feature, as indicated by the integrated peak areas in the initial and final spectra.

Finally, in situ gas-dosed powder x-ray diffraction data were collected for a sample of ZnH-MFU-4l to examine structural changes occurring upon CO<sub>2</sub> adsorption and desorption at elevated temperatures (see section 9.2 of the SM for details). Starting from a sample of activated ZnH-MFU-4l, diffraction patterns were collected during the course of heating from 25° to 300°C under flowing CO<sub>2</sub>. Upon increasing the temperature, beginning at ~100°C, noticeable increases were seen in the intensities of reflections at  $2\theta = 2.36^\circ$ ,  $3.65^\circ$ , and  $3.74^\circ$  (Fig. 3C and fig. S86), concomitant with an increase in the lattice parameter (as determined from Pawley fits to the data; fig. S91). A Rietveld refinement of the diffraction pattern collected at 300°C under CO<sub>2</sub> yielded a structure model consistent with Zn(O<sub>2</sub>CH)-MFU-4l (figs. S87 to S89). After cooling to 25°C under CO<sub>2</sub>, the sample was heated to 300°C under flowing He to regenerate ZnH-MFU-4l and then finally cooled under He. Rietveld refinements of the diffraction patterns allowed for analysis of the formate occupancy throughout the cycling, which supports the reversible interconversion of ZnH-MFU-4l and Zn(O<sub>2</sub>CH)-MFU-4l (fig. S90).

#### Adsorption performance under conditions relevant to industrial CO<sub>2</sub> capture

The high temperatures at which ZnH-MFU-4l captures CO<sub>2</sub> suggest that this material could be used to capture CO<sub>2</sub> directly from the exhaust streams from diverse point sources. To investigate this prospect further, we collected isothermal CO<sub>2</sub> adsorption-desorption cycling data for ZnH-MFU-4l at 300°C with adsorp-

tion under 200 mbar of pure CO<sub>2</sub>, selected to simulate capture from the flue gas generated by steel production (~20% CO<sub>2</sub> released at ~300°C) and regeneration under 20 mbar CO<sub>2</sub> (see fig. S27 for details) (45, 46). The material exhibited exceptional stability to long-term cycling under these conditions: After 508 cycles performed during the course of 150 hours, ZnH-MFU-4l retained >96% of its initial adsorption capacity (Fig. 2C). We found no comparable cycling data reported for any permanently porous materials in the literature.

Of note, TGA cycling data collected at 400°C (adsorption under 20% CO<sub>2</sub> in N<sub>2</sub> and desorption under pure N<sub>2</sub>; fig. S33) and at 300°C in the presence of O<sub>2</sub> (adsorption under 4% O<sub>2</sub>, 15% CO<sub>2</sub>, and 81% N<sub>2</sub> and desorption under pure N<sub>2</sub>; fig. S35) suggest that the material is robust under these more extreme conditions. We also collected preliminary cycling data to investigate the stability of ZnH-MFU-4l to water and SO<sub>2</sub>, two contaminants in many CO<sub>2</sub> exhaust streams (38, 39). Humid TGA cycling data collected for ZnH-MFU-4l with adsorption under a stream consisting of 20% CO<sub>2</sub> and 2% H<sub>2</sub>O in N<sub>2</sub> at 200°C and desorption under pure N<sub>2</sub> at 250°C revealed that although the CO<sub>2</sub> capacity after the 10th cycle (as determined by the quantity desorbed) was lower than that measured under equivalent dry cycling conditions (83% versus 95%, respectively), the material remained highly selective for CO<sub>2</sub> (see section 2.7.2 of the SM and figs. S38 to S40). Likewise, in situ DRIFTS data collected for ZnH-MFU-4l at 250°C during the course of 10 adsorption-desorption cycles involving adsorption under 21 ppm SO<sub>2</sub> and 20% CO<sub>2</sub> in N<sub>2</sub> and desorption under pure N<sub>2</sub> revealed that the framework is selective for CO<sub>2</sub> over SO<sub>2</sub> under these conditions. Indeed,

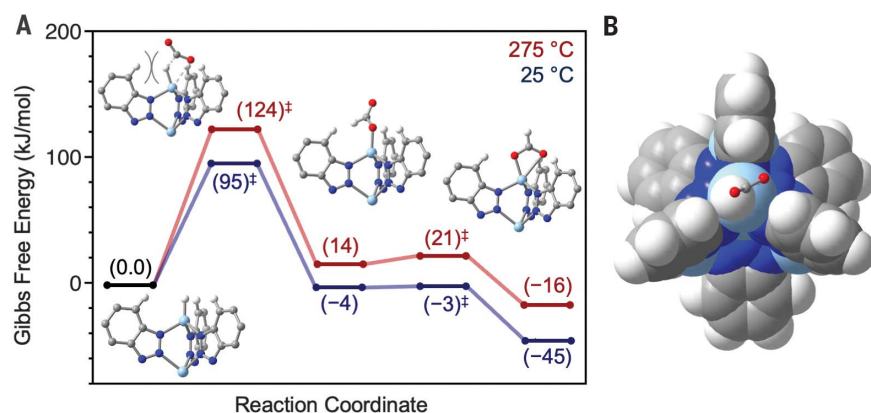


**Fig. 5. Calculated free-energy landscape for CO<sub>2</sub> insertion into the Zn–H bond.** (A) Free-energy landscape for the reaction of CO<sub>2</sub> with the model Zn<sub>5</sub>H<sub>4</sub>(bta)<sub>6</sub> cluster to yield Zn<sub>5</sub>(O<sub>2</sub>CH)<sub>4</sub>(bta)<sub>6</sub> at 25° and 275°C. The large barrier to CO<sub>2</sub> insertion (95 kJ/mol at 25°C) is consistent with the absence of CO<sub>2</sub> insertion reactivity at ambient temperature. At 275°C, there is still a large barrier to CO<sub>2</sub> insertion, but adsorption remains thermodynamically favored (see table S25), and high temperature provides enough thermal energy to overcome this barrier (see section 12 of the SM for computational details). (B) An overhead view of space-filling models illustrating the calculated transition state for CO<sub>2</sub> insertion into the Zn–H bond of Zn<sub>5</sub>H<sub>4</sub>(bta)<sub>6</sub>. As the CO<sub>2</sub> approaches the metal center, the hydride ligand is displaced and comes into close contact with one of the bta<sup>−</sup> ligands (distance of 2.42 Å, or approximately two times the van der Waals radius of hydrogen) (47). This unfavorable interaction likely contributes to the large activation barrier for CO<sub>2</sub> insertion.

during each cycle, adsorption resulted in the appearance of a broad stretch centered at 1611 cm<sup>−1</sup> diagnostic of the formation of Zn (O<sub>2</sub>CH)-MFU-4l, and exposure to flowing N<sub>2</sub> regenerated the spectrum for ZnH-MFU-4l (see fig. S79 and section 2.11 of the SM for details). After the 10th cycle, the integrated peak area for the  $\nu_{\text{Zn-H}}$  feature was ~97% of that determined for the spectrum of the pristine framework.

Finally, preliminary column breakthrough experiments were conducted to examine adsorption performance of pelletized ZnH-MFU-4l exposed to flowing 20 or 4% CO<sub>2</sub> (N<sub>2</sub> balance) at 280°C. Breakthrough data were first collected under flowing [10 standard cubic centimeters per minute (scm)] 20% CO<sub>2</sub> in N<sub>2</sub>, and the column was regenerated under flowing N<sub>2</sub> at 280°C until no CO<sub>2</sub> was detected at the outlet; additional breakthrough data were collected for the same sample under flowing (10 scm and then again at 20 scm) 4% CO<sub>2</sub> in N<sub>2</sub> (see section 2.8 of the SM for details and fig. S52). Sharp breakthrough of CO<sub>2</sub> occurred in under 10 and 30 min, respectively, when the sample was exposed to 20 or 4% CO<sub>2</sub> flowing at 10 scm (Fig. 2D; see fig. S52 for data collected under 20 scm 4% CO<sub>2</sub> in N<sub>2</sub>), and the material achieved a capture efficiency of >90% in both cases, corresponding to breakthrough capacities of 2.6 and 1.6 mmol/g, respectively. These results indicate that ZnH-MFU-4l is an extremely promising material for deep carbon capture at high temperature from dilute CO<sub>2</sub> streams.

#### Kinetics and free-energy landscape for CO<sub>2</sub> insertion

We investigated the kinetics of CO<sub>2</sub> adsorption in ZnH-MFU-4l from gas streams containing as little as 1.5% CO<sub>2</sub> in N<sub>2</sub> up to 100% CO<sub>2</sub> and at temperatures ranging from 160° to 300°C (Fig. 4A and figs. S44 to S47). Higher CO<sub>2</sub> concentrations and higher temperatures resulted in more-rapid adsorption kinetics and faster equilibration times (Fig. 4B). When exposed to a 20% CO<sub>2</sub> in N<sub>2</sub> stream at 300°C, ZnH-MFU-4l achieved 90% of the equilibrium CO<sub>2</sub> capacity (3.12 mmol/g) within 9 s (Fig. 4A). This capacity is similar to that determined from CO<sub>2</sub> isotherm measurements at 300°C and 200 mbar CO<sub>2</sub> (3.05 mmol/g). Variable-temperature kinetic traces for CO<sub>2</sub> adsorption (20% CO<sub>2</sub> in N<sub>2</sub>) and desorption (under N<sub>2</sub>) were satisfactorily modeled with a first-order rate law (Fig. 4C and figs. S49 and S50). Application of the Eyring equation afforded values for the entropy and enthalpy of activation at 298 K of  $\Delta H_{\text{ads}}^{\ddagger} = 54(4)$  kJ/mol and  $\Delta S_{\text{ads}}^{\ddagger} = -130(4)$  J/(mol·K), respectively, revealing a substantial entropic penalty associated with CO<sub>2</sub> activation. For the decarboxylation reaction, the activation enthalpy is very large, although the activation entropy is small [ $\Delta H_{\text{des}}^{\ddagger} = 130(4)$  kJ/mol and  $\Delta S_{\text{des}}^{\ddagger} = -21(4)$  J/(mol·K) at 298 K].

Density functional theory calculations performed on the model cluster Zn<sub>5</sub>H<sub>4</sub>(bta)<sub>6</sub> (bta<sup>−</sup> = benzotriazolate) yielded activation enthalpies and entropies for adsorption and desorption that are consistent with the experimental

values [ $\Delta H_{\text{ads}}^{\ddagger}(\text{calc}) = 60$  kJ/mol,  $\Delta S_{\text{ads}}^{\ddagger}(\text{calc}) = -116$  J/(mol·K), and  $\Delta H_{\text{des}}^{\ddagger}(\text{calc}) = 141$  kJ/mol,  $\Delta S_{\text{des}}^{\ddagger}(\text{calc}) = 1.8$  J/(mol·K); see section 12 of the SM and table S25]. Using the corresponding calculated Gibbs activation energies for CO<sub>2</sub> adsorption at 25° and 275°C ( $\Delta G_{\text{ads},25^{\circ}\text{C}}^{\ddagger} = 95$  kJ/mol,  $\Delta G_{\text{ads},275^{\circ}\text{C}}^{\ddagger} = 124$  kJ/mol; Fig. 5A) and taking a ratio of the Eyring equation solved at these temperatures (see section 6.4 in the SM), we found that the rate constant for CO<sub>2</sub> insertion at 275°C is five orders of magnitude greater than at 25°C, which serves to explain why CO<sub>2</sub> chemisorption occurs only at elevated temperatures. Notably, in the calculated transition state for CO<sub>2</sub> insertion, the hydride ligand comes into close contact with one of the benzotriazolate ligands, resulting in an unfavorable steric interaction that likely contributes to the large kinetic energy barrier (Fig. 5B).

#### Outlook

We have shown that the highly porous metal-organic framework ZnH-MFU-4l selectively and reversibly captures large quantities of CO<sub>2</sub> above 200°C, an operating temperature regime that is without precedent among intrinsically porous solids and introduces the prospect of using such materials for postcombustion CO<sub>2</sub> capture at elevated temperatures. More broadly, this work raises the prospect of designing reactive MOFs for the high-temperature capture of other industrially relevant gases, which could facilitate the replacement of energy-intensive schemes for other key separations or potentially even enable reaction temperatures to be lowered through adsorption enhancement.

#### REFERENCES AND NOTES

- S. Budinisi, S. Krevor, N. Mac Dowell, N. Brandon, A. Hawkes, *Energy Strategy Rev.* **22**, 61–81 (2018).
- Intergovernmental Panel on Climate Change, “Summary for policymakers” in *Climate Change 2021: The Physical Science Basis. Contribution of Working Group I to the Sixth Assessment Report of the Intergovernmental Panel on Climate Change* (Cambridge Univ. Press, 2021), pp. 3–32.
- International Energy Agency, “Renewables 2021: Analysis and Forecast to 2026” (IEA, 2021); <https://www.iea.org/reports/renewables-2021>.
- International Energy Agency, “World Energy Outlook 2022” (IEA, 2022); <https://www.iea.org/reports/world-energy-outlook-2022>.
- R. Quadrelli, S. Peterson, *Energy Policy* **35**, 5938–5952 (2007).
- S. J. Davis et al., *Science* **360**, eaas9793 (2018).
- G. T. Rochelle, *Science* **325**, 1652–1654 (2009).
- C.-H. Yu, C.-H. Huang, C.-S. Tan, *Aerosol Air Qual. Res.* **12**, 745–769 (2012).
- S. A. Mazari, B. S. Ali, B. M. Jan, I. M. Saeed, S. Nizamuddin, *Int. J. Greenh. Gas Control* **34**, 129–140 (2015).
- C. Halliday, T. A. Hutton, *Appl. Energy* **280**, 116016 (2020).
- H. Zhai, E. S. Rubin, *Environ. Sci. Technol.* **50**, 4127–4134 (2016).
- Y. Lara, A. Martínez, P. Lisbona, L. M. Romeo, *Energy Procedia* **114**, 2380–2389 (2017).
- H. Cui et al., *ACS Appl. Mater. Interfaces* **10**, 20611–20620 (2018).
- M. T. Dunstan, F. Donat, A. H. Bork, C. P. Grey, C. R. Müller, *Chem. Rev.* **121**, 12681–12745 (2021).
- V. S. Deresvischikov, A. I. Lysikov, A. G. Okunev, *Ind. Eng. Chem. Res.* **50**, 12741–12749 (2011).
- S. Mahajan, M. Lahtinen, *J. Environ. Chem. Eng.* **10**, 108930 (2022).



17. Z. Sharifzadeh, A. Morsali, *Coord. Chem. Rev.* **459**, 214445 (2022).
18. R. Vaidhyanathan *et al.*, *Science* **330**, 650–653 (2010).
19. J. B. Lin *et al.*, *Science* **374**, 1464–1469 (2021).
20. R. L. Siegelman, E. J. Kim, J. R. Long, *Nat. Mater.* **20**, 1060–1072 (2021).
21. E. J. Kim *et al.*, *Science* **369**, 392–396 (2020).
22. K. M. Waldie, A. L. Ostericher, M. H. Reineke, A. F. Sasayama, C. P. Kubiak, *ACS Catal.* **8**, 1313–1324 (2018).
23. E. S. Wiedner *et al.*, *Chem. Rev.* **116**, 8655–8692 (2016).
24. N. W. Kinzel, C. Werlé, W. Leitner, *Angew. Chem. Int. Ed.* **60**, 11628–11686 (2021).
25. D. Denysenko, M. Grzywa, J. Jelic, K. Reuter, D. Volkmer, *Angew. Chem. Int. Ed.* **53**, 5832–5836 (2014).
26. D. Denysenko *et al.*, *Chemistry* **17**, 1837–1848 (2011).
27. R. Röß-Ohlenroth, B. Breidenkötter, D. Volkmer, *Organometallics* **38**, 3444–3452 (2019).
28. A. Kreider-Mueller, P. J. Quinlivan, M. Rauch, J. S. Owen, G. Parkin, *Chem. Commun.* **52**, 2358–2361 (2016).
29. S. J. Datta *et al.*, *Science* **350**, 302–306 (2015).
30. S. Mukherjee *et al.*, *Sci. Adv.* **5**, eaax9171 (2019).
31. K. Sumida *et al.*, *Chem. Rev.* **112**, 724–781 (2012).
32. P.-Q. Liao *et al.*, *Energy Environ. Sci.* **8**, 1011–1016 (2015).
33. M. A. Alkhabbaz, P. Bollini, G. S. Foo, C. Sievers, C. W. Jones, *J. Am. Chem. Soc.* **136**, 13170–13173 (2014).
34. J. Xu *et al.*, *J. Phys. Chem. Lett.* **10**, 7044–7049 (2019).
35. H. J. Moon, J. M. Y. Carrillo, C. W. Jones, *Acc. Chem. Res.* **56**, 2620–2630 (2023).
36. J. A. Mason, K. Sumida, Z. R. Herm, R. Krishna, J. R. Long, *Energy Environ. Sci.* **4**, 3030–3040 (2011).
37. A. Lee *et al.*, *Energy Procedia* **4**, 1199–1206 (2011).
38. N. McQueen, C. M. Woodall, P. Psarras, J. Wilcox, in *Carbon Capture and Storage*, M. Bui, N. Mac Dowell, Eds., vol. 26 of *Energy and Environment Series* (The Royal Society of Chemistry, 2019), pp. 353–391.
39. T. P. Hills, M. G. Sceats, P. S. Fennell, in *Carbon Capture and Storage*, M. Bui, N. Mac Dowell, Eds., vol. 26 of *Energy and Environment Series* (The Royal Society of Chemistry, 2019), pp. 315–352.
40. R. E. James III *et al.*, “Cost and performance baseline for fossil energy plants, volume 3—low rank coal and natural gas to electricity,” 9th Annual International Pittsburgh Coal Conference (National Energy Technology Laboratory, 2022); <https://doi.org/10.2172/1888519>.
41. P. Schmieder *et al.*, *Dalton Trans.* **42**, 10786–10797 (2013).
42. E. D. Metzger *et al.*, *ACS Sustain. Chem. Eng.* **7**, 6654–6661 (2019).
43. F. Donat, C. R. Müller, *Curr. Opin. Green Sustain. Chem.* **36**, 100645 (2022).
44. M. E. Stoll, A. J. Vega, R. W. Vaughan, *Phys. Rev. A* **16**, 1521–1524 (1977).
45. G. S. Booras, S. C. Smelser, *Energy* **16**, 1295–1305 (1991).
46. A. B. Rao, E. S. Rubin, *Ind. Eng. Chem. Res.* **45**, 2421–2429 (2006).
47. S. S. Batsanov, *Inorg. Mater.* **37**, 871–885 (2001).

## ACKNOWLEDGMENTS

Certain commercial equipment, instruments, or materials are identified in this document. Such identification does not imply recommendation or endorsement by the National Institute of Standards and Technology (NIST), nor does it imply that the products identified are necessarily the best available for the purpose. The views expressed in the article do not necessarily represent the views of the US Department of Energy (DOE) or the US Government. The US Government retains and the publisher, by accepting the article for publication, acknowledges, that the US Government retains a nonexclusive, paid-up, irrevocable, worldwide license to publish or reproduce the published form of this work, or allow others to do so, for US Government purposes. We thank A. Yakovenko (Argonne National Laboratory) for technical assistance with powder x-ray diffraction data refinement, and J. L. Peltier, B. E. R. Snyder, and J. Börgel (University of California, Berkeley) for helpful discussions. **Funding:** Gas adsorption analyses and the spectroscopic characterization of materials were supported by the US DOE, Office of Basic Energy Sciences, Separation Science in the Chemical Sciences, Geosciences, and Biosciences Division, under award DE-SC0019992. The synthesis of materials and computational efforts were supported by the Hydrogen Materials–Advanced Research Consortium (HyMARC), established as part of the Energy Materials Network under the US DOE, Office of Energy Efficiency and Renewable Energy, Hydrogen and Fuel Cell Technologies Office, under contract DE-AC02-05CH11231. We further acknowledge fellowship support from the NASA Space Technology Graduate Research Opportunity program (R.C.R.), the Arnold and Mabel Beckman Foundation (K.M.C.), and the National Science Foundation Graduate Research Fellowship program (M.N.D.). J.R.L. acknowledges support from the Miller Institute for Basic Research in Science at the University of California, Berkeley. This research used resources of the Advanced Photon Source, a DOE Office of Science user facility operated for the DOE Office of Science by Argonne National Laboratory under contract DE-AC02-06CH11357. R.A.K. gratefully acknowledges support from the US DOE Office of Energy Efficiency and Renewable Energy, Hydrogen and Fuel Cell Technologies Office contract DE-AC36-8G028308 to the National Renewable Energy Laboratory. Part of this work was supported by NIST. This research also used resources of the National Energy Research Scientific Computing Center (NERSC), a US DOE Office of Science User Facility located at Lawrence Berkeley National Laboratory, operated under contract DE-AC02-05-CH11231 using NERSC award BES-ERCAP-0023680. Electron microscopy was supported by the US DOE, Office of Science, Basic Energy Sciences, Materials Sciences and Engineering Division under contract DE-AC02-05-CH11231 within the Electron

Microscopy of Soft Matter Program (KC11BN). Work at the Molecular Foundry was supported by the Office of Science, Office of Basic Energy Sciences, of the US DOE under contract DE-AC02-05CH1123. Computational modeling was supported by the Director, Office of Science, Office of Basic Energy Sciences, of the US DOE through the Gas Phase Chemical Physics Program, under contract DE-AC02-05CH11231. A portion of this research used resources at the High Flux Isotope Reactor, a DOE Office of Science User Facility operated by the Oak Ridge National Laboratory. **Author contributions:** R.C.R., K.M.C., and J.R.L. formulated and directed the research. R.C.R. and K.M.C. synthesized materials, conducted isotherm and isobar measurements, and analyzed the data. R.C.R., K.M.C., and M.N.D. conducted and interpreted kinetics measurements. H.K., A.J.H., K.M.C., and J.W.T. assisted in the collection and refinement of single-crystal x-ray diffraction data. H.Z.H.J., R.A.K., S.L.K., Y.W., Y.Y., K.C.B., K.E.E., A.M.M., J.A.R., and C.M.B. conducted spectroscopic characterization. R.A.K. and C.M.B. collected and analyzed powder x-ray diffraction data. D.R.Y., R.A.K., and C.M.B. collected and analyzed powder neutron diffraction data. M.N.D. collected and interpreted breakthrough data. H.F. collected and interpreted pycnometer density measurements. A.R.M., N.V.T., and M.H.-G. performed computational analyses. R.C.R., K.M.C., and K.R.M. drafted the manuscript. All authors contributed to revision of the manuscript. **Competing interests:** The University of California, Berkeley, has applied for a patent on some of the technology discussed herein regarding high-temperature gas capture with porous materials, on which R.C.R., K.M.C., and J.R.L. are listed as co-inventors. **Data and materials availability:** The supplementary materials contain complete experimental and spectral details for all new compounds reported herein. Crystallographic data for solid-state structures obtained from single-crystal x-ray diffraction have been made available free of charge from the Cambridge Crystallographic Data Centre (CCDC) under deposition numbers 2250026 (ZnEt-MFU-4l), 2250025 (Zn(O<sub>2</sub>CH)-MFU-4l), 2250027 (ZnH-MFU-4l), and 2166411 [CO<sub>2</sub>-derived Zn(O<sub>2</sub>CH)-MFU-4l]. Data for solid-state structures obtained from powder synchrotron x-ray and neutron diffraction data have been additionally deposited to the CCDC with deposition numbers 2263702–2263708 and 2352001. **License information:** Copyright © 2024 the authors, some rights reserved; exclusive licensee American Association for the Advancement of Science. No claim to original US government works. <https://www.science.org/about/science-licenses-journal-article-reuse>

## SUPPLEMENTARY MATERIALS

[science.org/doi/10.1126/science.adk5697](https://science.org/doi/10.1126/science.adk5697)  
Materials and Methods  
Figs. S1 to S128  
Tables S1 to S26  
References (48–94)

Submitted 29 August 2023; resubmitted 22 June 2024  
Accepted 23 September 2024  
[10.1126/science.adk5697](https://doi.org/10.1126/science.adk5697)